Dependence of seismoelectric amplitudes on water content

Matthias Strahser,[1,2] Laurence Jouniaux,[1] Pascal Sailhac,[1] Pierre-Daniel Matthey[1] and Matthias Zillmer[1]

[1]*Institut de Physique du Globe de Strasbourg,* CNRS-UMR7516, *Université de Strasbourg, 5 rue R. Descartes, 67084 Strasbourg, France. E-mail: mstrahser@geophysik.uni-kiel.de*

[2]*Institut für Geowissenschaften, Abteilung Geophysik, Christian-Albrechts-Universität zu Kiel, Otto-Hahn-Platz 1, 24118 Kiel, Germany*

SUMMARY

The expectation behind seismoelectric field measurements is to achieve a combination of the sensitivity of electrical properties to water content and permeability and the high spatial resolution of seismic surveys. A better understanding of the physical processes and a reliable quantification of the conversion between seismic energy and electric energy are necessary, and need to take into account the effect of water content, especially for shallow subsurface investigations. We performed a field survey to quantify the seismoelectric signals as the water content changed. We measured seismoelectric signals induced by seismic wave propagation, by repeating the observations on the same two profiles during several months. The electrical resistivity was monitored to take into account the water content variations.

We show that the horizontal component of the seismoelectric field, normalized with respect to the horizontal component of the seismic acceleration is inversely proportional to the electrical resistivity $\rho^{0.42 \pm 0.25}$. Assuming that the observed resistivity changes depend only on the water content, this result implies that the electrokinetic coefficient should increase with increasing water saturation. Taking into account the water saturation and combining our results with the Archie law for the resistivity in non-saturated conditions, the normalized seismoelectric field is a power-law of the effective saturation with the exponent $(0.42 \pm 0.25)n$ where n is Archie's saturation exponent.

Key words: Numerical approximations and analysis; Electrical properties; Hydrogeophysics; Body waves; Wave propagation; Acoustic properties.

1 INTRODUCTION

Transient seismoelectric phenomena can be caused by seismic waves in porous media through electrokinetic coupling and measured in the form of an electric potential difference between the electrodes of a dipole. Two kinds of seismoelectric effects are to be distinguished. The dominant contribution we are addressing in this paper corresponds to the electrical coseismic field accompanying the body and surface waves. The second kind is generated at contrasts of physico-chemical properties and consists of independently propagating electromagnetic waves (see, e.g. Haartsen & Pride 1997). Garambois & Dietrich (2002) showed in a numerical study that these signals are created at contrasts in porosity, permeability, salinity and viscosity.

Seismoelectric phenomena are especially appealing to hydrogeophysics because of their potential to characterize reservoirs and the fluids contained in the reservoir rocks with the resolution of seismic methods. Indeed seismoelectric tomography could connect the sensitivity of electrical properties to water content and permeability with the high spatial resolution of seismic surveys. To develop the potential of this innovative method, a better understanding of the

physical processes and a reliable quantification of the conversion between seismic energy and electric energy are necessary. Moreover a suitable interpretation of the observations, especially in the shallow subsurface, needs to take into account the water content as well as the rock and water conductivities.

Electrical methods, including resistivity or self-potential, have been studied either in laboratory (Jouniaux *et al.* 1994; Pozzi & Jouniaux 1994; Henry *et al.* 2003; Jouniaux *et al.* 2006) or in the field (Sill, 1983; Aubert & Atangana 1996; Perrier *et al.* 1998; Jouniaux *et al.* 1999; Gibert & Pessel, 2001; Pinettes *et al.* 2002; Sailhac *et al.* 2004; Saracco *et al.* 2004; Minsley *et al.* 2007; Maineult *et al.* 2008). Over the past decades, field experiments were conducted to characterize the seismoelectric phenomena (Thompson 1936; Martner & Sparks 1959; Long & Rivers 1975). Successful field experiments performed in recent years (Garambois & Dietrich 2001; Thompson *et al.* 2005; Dupuis *et al.* 2007; Strahser *et al.* 2007; Haines *et al.* 2007a,b; Dupuis *et al.* 2009) have stimulated new interest in this particular mechanism.

As described by Pride (1994), an analytical interpretation of these phenomena needs to connect the theory of Biot (1956) for the seismic wave propagation in a two-phase medium with Maxwell's

equations, using dynamic electrokinetic couplings. These analytical developments opened the possibility to numerically simulate these electrokinetic coupling phenomena—which involves the so-called electrokinetic coefficient—in homogeneous or layered saturated media (Haartsen & Pride 1997; Haartsen *et al.* 1998; Garambois & Dietrich 2001, 2002) with applications to reservoir geophysics (Saunders *et al.* 2006).

These theoretical developments showed that the seismoelectric coupling is dependent on the fluid conductivity and the electric double layer (the electrical interface between the grains and the water). This seismoelectric coupling can be quantified directly through seismoelectric measurements, or using laboratory investigations on the steady-state electrokinetic coefficient (C_s). Most of the field experiments are performed in the shallow subsurface for hydrological applications, meaning at various water contents, a parameter which is not taken into account up to now, neither in theory nor in measurements. Moreover, although the amplitude of the signals is often mentioned (Martner & Sparks 1959; Butler 1996; Hunt & Worthington 2000; Garambois & Dietrich 2001; Dupuis & Butler 2006), it is not usually studied by numerical studies, although it could be used to image the geometry of hydrocarbon reservoirs (Thompson *et al.* 2007).

This paper describes a field study, performed on two field sites named 'La Soutte' and 'Champ du Feu' in the Vosges Mountains, East of France. The main goal of these experiments was to repeatedly measure the amplitude of the seismoelectric field at the surface as the water content changes. These signals were monitored during the seismic wave propagation induced by hammer shots. We also measured the electrical resistivity to follow the water content changes. These observations were repeated several times in the summer of 2008 on the same two profiles. The hydrology of the site did not change drastically during experiments and the water table variations are not thought to induce variations in solutes. We show through these field measurements that the seismoelectric signals were affected by the water content. Taking into account the water saturation and assuming the Archie law for the resistivity in non-saturated conditions, the normalized seismoelectric field is a power-law of the effective saturation with the exponent $(0.42 \pm 0.25)n$ (see eq. 17).

2 SEISMIC TO ELECTROMAGNETIC CONVERSION: THEORETICAL BACKGROUND

2.1 Pride's theory

The equations governing the coupled seismic and electromagnetic wave propagation in a fluid-saturated porous medium have been developed by Pride (1994). Two transport equations express the coupling between the mechanical and electromagnetic wavefields (eqs 174, 176 and 177 in Pride 1994):

$$\mathbf{J} = \sigma(\omega)\mathbf{E} + L(\omega)\left(-\nabla p + i\omega^2 d_f \mathbf{u_s}\right) \qquad (1)$$

$$-i\omega\mathbf{w} = L(\omega)\mathbf{E} + \frac{k(\omega)}{\eta}\left(-\nabla p + i\omega^2 d_f \mathbf{u_s}\right). \qquad (2)$$

In eq. (1), the macroscopic electrical current density **J** is written as the sum of the average conduction and streaming current densities. Similarly, the fluid flux **w** of eq. (2) is separated into electrically and mechanically induced contributions. The electrical fields and

mechanical forces that generate the current density **J** and fluid flux **w** are **E** and $(-\nabla p + i\omega^2 d_f \mathbf{u_s})$, respectively, where p is the pore-fluid pressure and $\mathbf{u_s}$ the solid displacement. In the above relationships, d_f is the pore-fluid density, η is the shear viscosity of the fluid and ω is the angular frequency. The most important parameter in eqs (1) and (2) is the complex and frequency-dependent electrokinetic coupling $L(\omega)$, which describes the coupling between the seismic and electromagnetic fields (Pride 1994; Reppert *et al.* 2001). The remaining two coefficients, $\sigma(\omega)$ and $k(\omega)$, represent the electric conductivity and dynamic permeability of the porous material, respectively.

2.2 The electric double layer

The electrokinetic coupling phenomena are created at the microscopic scale when there is a relative motion of electrolyte ions with respect to the mineral surface. Minerals forming the rock develop an electric double layer when in contact with an electrolyte, usually resulting from a negatively charged mineral surface. An electric field is created perpendicular to the mineral surface which attracts counterions (usually cations) and repulses anions in the vicinity of the pore–matrix interface. The electric double layer is made up of the Stern layer, where cations are adsorbed on the surface, and the Gouy diffuse layer, where the number of counterions exceeds the number of anions (for a detailed description see Adamson 1976; Hunter 1981). The streaming potential is due to the motion of the diffuse layer induced by a fluid pressure difference along the interface. The zeta potential is defined at the slipping plane or shear plane (i.e. the potential within the double layer at the zero-velocity surface) and depends on rock matrix, fluid composition, *pH*, and temperature (Davis *et al.* 1978; Ishido & Mizutani, 1981; Lorne *et al.* 1999; Jouniaux *et al.* 2000; Guichet & Zuddas, 2003; Reppert & Morgan 2003a,b; Guichet *et al.* 2006).

2.3 Seismoelectric coupling

Seismic wave propagation in fluid-filled porous media generates conversions from seismic to electric and electromagnetic energy, which can be observed at the macroscopic scale, due to this electrokinetic coupling at the pore scale. The complete theoretical treatment of seismoelectric couplings in unsaturated media has not been performed yet. Indeed, it is necessary to combine an extension of Biot's theory for partially saturated conditions with the water content dependence of the dynamic electrokinetic coupling, which is not really understood.

The seismoelectric coupling is complex and frequency-dependent (Pride 1994). It describes the coupling between the seismic and electromagnetic fields.

$$L(\omega) = L_{ss}\left[1 - i\frac{\omega}{\omega_c}\frac{m}{4}\left(1 - 2\frac{d}{\Lambda}\right)^2\left(1 - i^{3/2}d\sqrt{\frac{\omega d_f}{\eta}}\right)^2\right]^{-\frac{1}{2}},$$

(3)

where L_{ss} is the steady-state electrokinetic coupling, ω_c is the transition frequency separating low-frequency viscous flow and high-frequency inertial flow, d is related to the Debye length, Λ is a porous-material geometry term and m is a dimensionless number (details in Pride 1994). Some laboratory experiments have been performed on dynamic seismoelectric conversions (Packard 1953; Cooke 1955; Chandler 1981; Mironov *et al.* 1994; Reppert *et al.* 2001; Bordes *et al.* 2006, 2008; Schoemaker *et al.* 2008), some

of them focusing on laboratory borehole measurements (Zhu *et al.* 1999; Zhu & Toksöz 2003). Recently Chen & Mu (2005) as well as Block & Harris (2006) confirmed by laboratory experiments that a seismic wave crossing an interface induces an electromagnetic field, with electrokinetic origin, by measuring the associated electric field.

Garambois & Dietrich (2001) studied the low-frequency assumption valid at seismic frequencies, meaning at frequencies where $\omega \ll \omega_c$, with

$$\omega_c = \frac{\phi}{\alpha_\infty k_0} \frac{\eta}{d_f}, \tag{4}$$

where k_0 is the intrinsic permeability, ϕ the porosity and α_∞ the tortuosity. Note that the porosity divided by the tortuosity is equal to the inverse of the formation factor, itself equal to the fluid conductivity divided by the rock conductivity. Garambois & Dietrich (2001) gave the coseismic transfer function for longitudinal plane waves. In this case, they showed that the seismoelectric field E is proportional to the grain acceleration.

$$\mathbf{E} \simeq -\frac{L_{ss}}{\sigma_r} d_f \ddot{\mathbf{u}}, \tag{5}$$

where σ_r is the rock conductivity.

A direct investigation of the dependence of the seismoelectric amplitude on water content is to measure the seismoelectric field and the soil acceleration, and to deduce the transfer function. In laboratory, seismoelectric measurements have been performed using an ultrasonic source, from hundreds of hertz to a few tens of kilohertz. It has been shown that the seismoelectric effect depends on lithology, structure and texture of rocks and their fluid saturations (Ageeva *et al.* 1999). A characteristic decrease of the seismoelectric effect is observed with increasing salinity, at full saturation on limestones and sandstones (Ageeva *et al.* 1999), and at water contents of 8 per cent or 24 per cent on sand (Parkhomenko & Gaskarov 1971); a decrease with increasing porosity is also observed (Ageeva *et al.* 1999). The seismoelectric effect shows a sharp increase at low water content, and can then be constant at increasing water content on dolomite, marl and sandstones, or can decrease on tegillate loam, morainic loam and limestones (Parkhomenko & Tsze-San 1964; Parkhomenko & Gaskarov 1971; Ageeva *et al.* 1999). However, at low frequencies (400 Hz compared to 25 kHz) no decrease of the seismoelectric effect is observed with increasing water saturation. It is difficult to conclude about the behaviour of the seismoelectric effect with water saturation that could be applied in the field. Only Ageeva *et al.* (1999) performed measurements at low frequencies (400 Hz), but they normalize the seismoelectric signal to the response of the source of the elastic waves (the test transducer, in V), so that the coseismic transfer function (eq. 5) cannot be deduced.

A non-direct investigation of this problem would be to try to deduce the transfer function by determining L_{ss}, σ_r and d_f and then use eq. (5).

2.4 Electrokinetic coefficient

The steady-state electrokinetic coefficient can be expressed as

$$C_s = -\frac{L_{ss}}{\sigma_r} = \frac{\Delta V}{\Delta P} = \frac{\epsilon \zeta}{\eta \sigma_f}, \tag{6}$$

where σ_f and ϵ are the fluid conductivity and the dielectric constant of the fluid, and ζ is the zeta electrical potential (within the double layer at the interface between the rock and the fluid). The steady-state electrokinetic coefficient can be measured in laboratory, by applying a fluid flow (ΔP) and by measuring the induced electric

potential (ΔV) (Jouniaux *et al.* 2000; Guichet *et al.* 2006; Jaafar *et al.* 2009).

It has been proposed (Darnet & Marquis, 2004; Sailhac *et al.* 2004) that the electrokinetic coefficient depends on the effective saturation as follows:

$$C_s = \frac{\Delta V}{\Delta P} = \frac{\epsilon \zeta}{\eta \sigma_f S_e^n}, \tag{7}$$

where n is the Archie saturation exponent. This implies that when the effective saturation S_e is decreased, the electrokinetic coefficient is increased. However the few observations published up to now do not show this behaviour (Guichet *et al.* 2003). Based on laboratory studies Guichet *et al.* (2003) proposed that the electrokinetic coefficient increases with water content as

$$C_s = \frac{\Delta V}{\Delta P} = \frac{\epsilon \zeta S_e}{\eta \sigma_f}. \tag{8}$$

To clear this ambiguity we propose to directly measure the seismoelectric coefficient through field experiments, meaning the coseismic transfer function between the seismoelectric field and the acceleration (eq. 5). Besides the acceleration, transient seismoelectric amplitudes ($\mathbf{E}$ in eq. 5) will be affected by electrokinetic coefficient variations, fluid conductivity, as well as fluid viscosity or fluid density variations. To keep all these parameters constant, we chose to repeat our seismoelectric observations on the same two profiles, so that the possibly observed variations could be attributed to the water content changes of the field.

3 FIELD OBSERVATIONS

3.1 Fields La Soutte and Champ du Feu

Two profiles were investigated: 'La Soutte' and 'Champ du Feu' located in the Vosges mountains (northeast of France). Both sites La Soutte and Champ du Feu are underlain by volcanic and crystalline rocks forming the geotectonic units of mid-European Variscides (or Hercynian). High-grade metamorphic sequences were formed and intruded by numerous granitoid plutons. Thick friable weathered plutonic and volcanic rocks are overlain by gravelly sandy-silty solifluction deposits on which a palaeosoil profile, no more than 3 m, has developed.

La Soutte is a six hectare glade that contains the source of the Ehn river near the crest (at 950 m altitude). The solifluction deposits are not homogeneous on the entire six hectare glade, but are homogeneous at the scale 50 cm to 1 m at the top of this catchment area, where we performed the measurements (Sailhac *et al.* 2009). The depth to the top of the shallow aquifer is small (zero at some locations) and variable in space ($\approx$3 m amplitude, with max slope of $\approx$1/20) and time ($\approx$1 m amplitude through seasons). It is monitored using continuous measurements in boreholes: DIVER probes from Schlumberger Water Services (four piezometric level sensors and temperature sensors, and a BARO probe for the atmospheric pressure correction). Weather conditions are monitored as well, with temperature, hygrometry, solar radiation, anemometry and precipitation. The site also involves continuous self-potential measurements (network of 40 unpolarizable electrodes). In addition, the ambient electromagnetic noise is also monitored through a three-component magnetic observatory located at 10 km distance (in Welschbruch). The area has been previously characterized through well-logging (slug tests, geophysics and geochemistry in boreholes) and surface geophysics (electric tomography and refraction seismics,
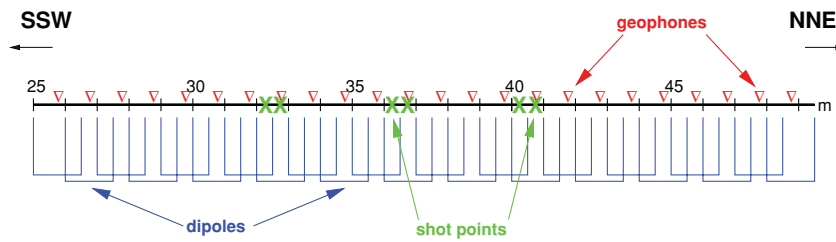
Figure 1. Measurement layout: the seismic source (green) is a hammer, the geophones (red) are located in the middle of the respective electrical dipole (blue).

but also magnetic mapping, audio-electromagnetic soundings, nuclear magnetic resonance soundings and ground penetrating radar, Sailhac *et al.* 2009).

The Champ du Feu site has also been studied with several geophysical prospection methods: seismic, electric, magnetic, radar and self-potential (Gorsy *et al.* 2006). The soil is altered up to 2–5 m depth, above a volcanic and granodiorite bedrock. The profile is located on a slope, with a little stream downwards at about 50 m from the profile, and a small depth to the shallow aquifer. The electrical resistances measured at each dipole are relatively constant along the profile and in general a little bit lower than those observed in La Soutte though still quite similar. The previous studies on these fields allowed us to choose the appropriate place to perform measurements by repeating the same profiles.

3.2 Experimental methodology

The field setup of the seismoelectric method comprises elements of both seismics and geoelectrics: A seismic signal is generated, in our case with a sledge hammer hitting a metal plate. The signal travels through the Earth and creates electrical signals (see Section 1). These are picked up by dipoles consisting of two electrodes between which the electric potential difference is measured using pre-amplifiers. Analogously to a seismic profile with several geophones being connected to a seismic recording unit to measure ground velocity, we use a seismoelectric profile of 24 dipoles to record the electric signals generated by a seismic compressional wave. Since these dipoles output a voltage, just as a geophone does, we can connect them to a seismic recording unit, too. In La Soutte, the investigated profile is 25 m long, with 1.5-m-long dipoles (40-cm-long brass electrodes), and 1 m distance between the dipoles. In other geophysical methods where one needs accurate measurements of time variations of the electric field, using unpolarizable electrodes is often necessary: this is the case for instance in MT (magnetotellurics) at low frequencies (<20 Hz) but also in Audio-MT where the frequency band (20 Hz–20 kHz) includes those used in seismoelectric records (20–200 Hz). Investigations by Beamish (1999) showed that seismoelectric signals obtained with

polarizable or non-polarizable electrodes do not differ significantly from one another. Earlier tests by one of the authors (M. Strahser) yielded the same result. Thus these experiments show that the electrode polarization is less of a problem in seismoelectric than in other geophysical methods such as AMT. A geophone is placed in the middle of each dipole to simultaneously measure the seismic signals. We carried out several tests to ensure that the geophones do not influence the seismoelectric recordings. We first used vertical geophones, and when all shotpoints had been measured, the vertical geophones were replaced with horizontal ones and the measurements were repeated. The source is a hammer shot on a metallic plate. We usually move the shot point to six positions within the profile (see Fig. 1).

Presuming that the parameters of the ground do not change significantly over a 0.5 m scale, we can easily double the amount of traces by adding the traces of two adjacent shotpoints: The first shotpoint yields seismic and seismoelectric traces with offsets of ± 1 m, ± 2 m, ..., ± 12 m. If we move the shotpoint 0.5 m inline and keep the receivers constant, we get traces at 0.5 m, ± 1.5 m, ± 2.5 m, ... distance. Adding the traces of these shots results in offsets of 0.5 m, ± 1 m, ± 1.5 m, ± 2 m... . Fig. 2 exemplifies how well this technique works. The traces recorded at the first shotpoint are drawn in red, the ones from the second shotpoint in black. They fit accurately together.

Pre-amplifiers are used for the electric acquisition (from Kiel University, Germany, manufactured by GeoServe, Kiel), leading to an amplification factor of six. We used a Geometrics Strataview for the acquisition of seismic and seismoelectric signals. The automatic trigger is not used because it induces an electrical noise at time zero that perturbs the seismoelectric signal. We used a manual trigger with a geophone located at 3 m crossline difference from the shot plate, whose first arrival was calibrated with the automatic trigger (using four stacks). A cross-correlation of the manually triggered geophone traces with the automatically triggered ones yields the time differences, which the manually triggered records have to be corrected with to get the real zero times. For each shot location the electrical data are stacked 20 times. Because of the manual trigger, we had to choose a long recording length (1024 ms). The sampling frequency was set to 4 kHz (sampling period 250 μs) which allows
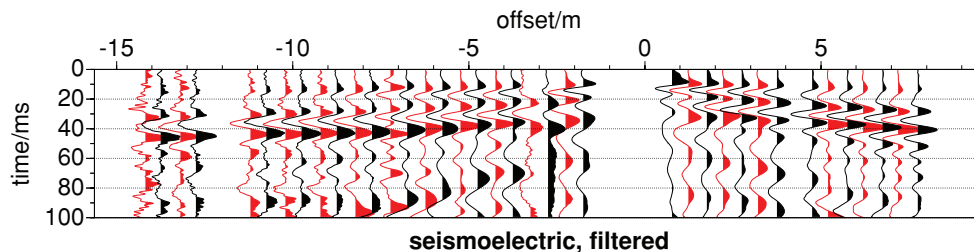

Figure 2. The amount of traces can be doubled by adding the traces of two adjacent shotpoints, in this case yielding dipole distances of 0.5 m. The traces from the first shotpoint are in red, the traces from the second one in black.
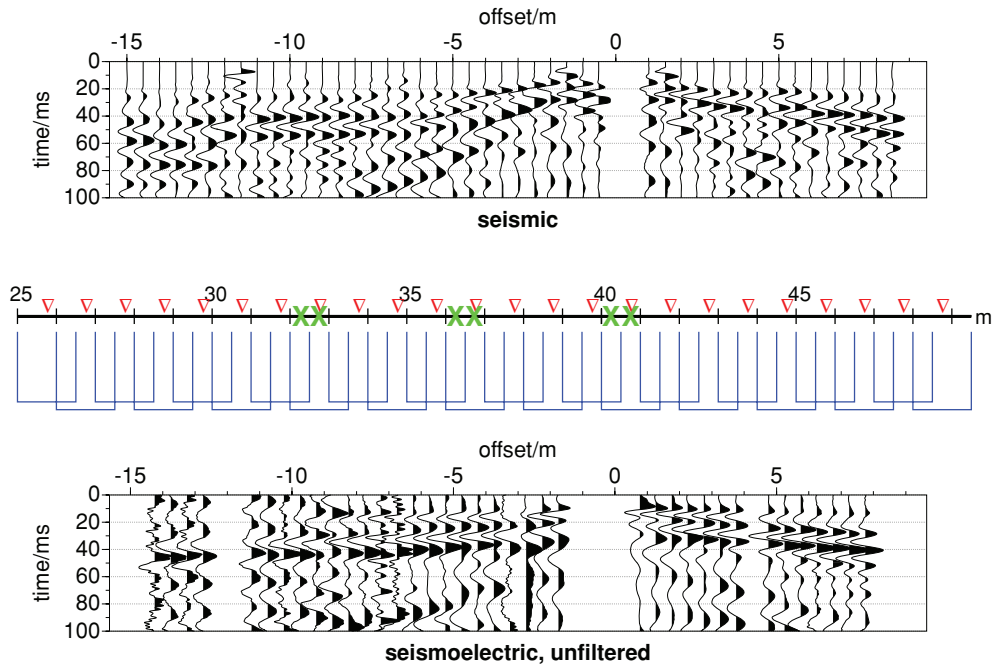
Figure 3. Seismoelectric and seismic signals measured along the profile at La Soutte (raw data). The shotpoint is located at distance zero. Top panel: geophone recordings (vertical component), middle panel: measurement layout (see annotations in Fig. 1), bottom panel: dipole recordings. The data are agc-scaled. Noisy traces were discarded from the records.

accurate picking of the first arrivals. A bandpass filter (5–500 Hz) was applied later to minimize low- and high-frequency noise.

The water content was monitored by electrical resistance measurements. We measured the electrical resistance between the two electrodes of each dipole at a frequency of 25 Hz, using a home-made apparatus with an input impedance of 100 MΩ. Since the electrical conductivity of the water present in the field does not change significantly, the electrical resistance changes are attributed only to water content changes. The values measured at surface streams and within the borehole closest to the measurement area, and at different dates, are in the range of 5–6 mS m^{-1} with a pH in the range of 6–7 (Sailhac *et al.* 2009). The same methodology is used at Champ du Feu. We include data from both locations to get a broader database, especially a larger variation of the measured resistances. Since the upper decimetres of the soil were quite similar at both locations, we assume that combining data from these two areas does not cause significant errors.

4 RESULTS

4.1 Typical observations of seismics, seismoelectrics and resistivity

An example of results from La Soutte is shown in Fig. 3 with the seismic signals recorded by the vertical geophones on the top of the figure, and the seismoelectric signals recorded by the electrical dipoles at the bottom. A typical velocity of the seismoelectric first arrival at some metres offset from the source is 1230 m s^{-1}, which corresponds to the velocity of the seismic refracted wave. It is probably refracted at a small local aquifer of strongly weathered volcanic rocks (medium grain sand) or perhaps at a zone close to such an aquifer and connected with it via fractures since the velocity is rather small for an aquifer (for more details about La Soutte, see

Sailhac *et al.* 2009). Note that we applied a polarity correction to the seismic and seismoelectric horizontal component data so that the two sides of the profile can be compared with one another more easily, that is, we do not have a change of polarity from one side of the shotpoint to the other. Note also that the seismic and the seismoelectric traces are not at the same positions, since the geophones are positioned in the middle of each dipole. For the seismoelectric trace, the position of the dipole electrode which is closer to the source is taken as position. To remove the 50 Hz noise and its harmonics, the seismoelectric data are filtered by subtracting sinusoids adapted in amplitude, phase and frequency to best fit the data (Adam & Langlois 1995): It is assumed that the noise is of the form

$$n(t) = A \sin(\omega t) + B \cos(\omega t). \tag{9}$$

The parameters A and B can be estimated from the data:

$$\tilde{A} = \frac{2}{n} \sum a_t \sin(\tilde{\omega} t), \quad \tilde{B} = \frac{2}{n} \sum a_t \sin(\tilde{\omega} t), \tag{10}$$

with $\tilde{A}$ and $\tilde{B}$ being the estimates of amplitudes A and B, $\tilde{\omega}$ the estimated frequency and a_t the data points of the time-series. Since 50 Hz noise can actually deviate by several megahertz, the amplitudes are evaluated at small frequency increments around the initially guessed frequency. The frequency corresponding to the largest amplitude is then used for the sinusoid subtraction. The filtered result is shown in Fig. 4. Similar techniques are described in Butler & Russell (1993, 2003). The effect is equivalent to a very narrow notch filter but the filter works in the time-space domain. A transformation to and from the frequency–wavenumber domain would cause artefacts due to the Gibbs phenomenon.
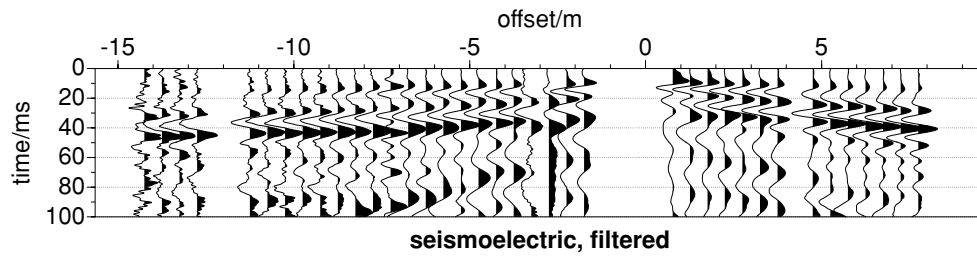
Figure 4. Seismoelectric signals filtered by subtracting sinusoids adapted in amplitude, phase and frequency to the data. The unfiltered data are shown in Fig. 3.

4.2 Amplitude analysis

To pick the maximum amplitude of the signal, we define a time window in which we automatically detect the maximum of the envelope of the first arrival on every trace. The time window is defined on the seismoelectric signals first, and the same time window is used for the seismic records (see Fig. 5). For a reason that we could not explain, the first arrival of the seismoelectric signals is recorded before the first arrival of the seismic records, in the filtered data (Fig. 5) as well as in the raw data (Fig. 3). Such a feature is not usual. Therefore we compared the time-response of our geophones to the time-response of several other geophones, and we checked the bandpass filter of our geophones, but could not find any explanation to this time delay. This phenomenon was not encountered in other seismoelectric measurements done before by one of the authors (Strahser 2007). It cannot be explained by spatial offsets between electrodes and geophones. If we assume a spatial offset of 10 cm and take the typical velocity of 1250 m s^{-1}, the temporal offset would be 0.08 ms, while we observe temporal offsets of more than 10 ms. This would correspond to an offset of more than 10 m. Noisy traces were excluded from the analysis, as well as traces with exceedingly high or low amplitudes.

We plotted the maximum amplitude of the envelope of the seismic and seismoelectric records as a function of the distance from
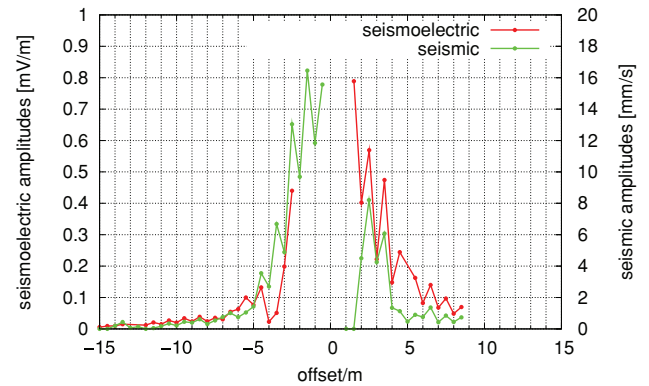

Figure 6. Maximum amplitude of the seismic (vertical geophones) and seismoelectric signals. The traces very close to the source are not included.

the source in Fig. 6 . As expected, the (seismically induced) particle velocity decreases far from the source. Therefore the induced seismoelectric signal decreases, too (see eq. 5). Note that the seismoelectric signal is up to 0.8 mV m^{-1} near the source, and only around 50 μV m^{-1} at 5–7 m from the source. One can also see that the summing up of two adjacent shots was not perfect here because there is a clear zigzag pattern in the amplitudes.
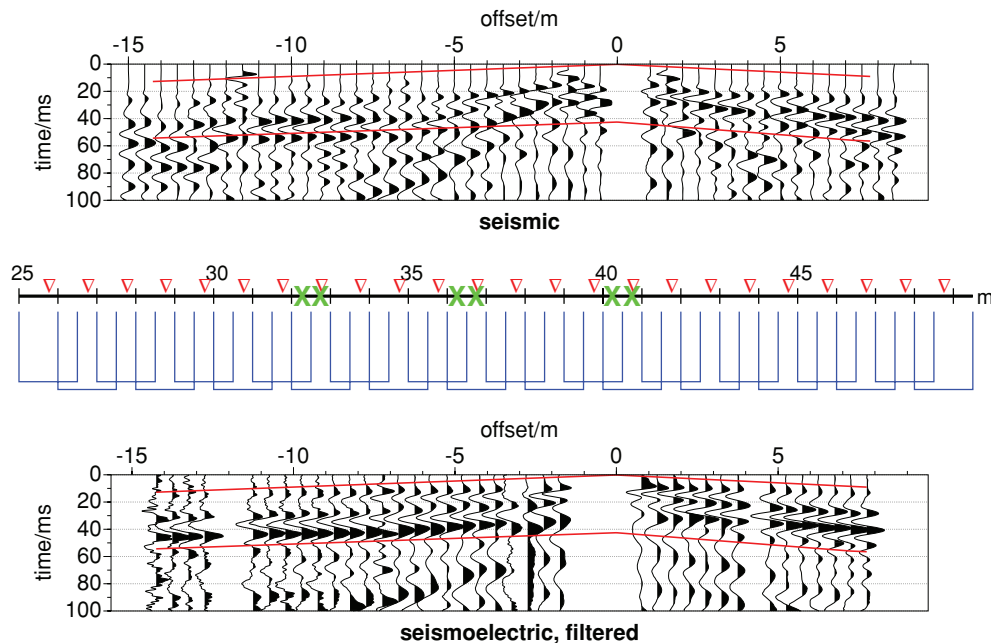

Figure 5. One example of seismic (velocity) and seismoelectric signals with the chosen time window in which the maximum of the envelope is picked automatically. Top panel: geophone recordings (vertical component), bottom panel: dipole recordings. The data are agc-scaled.

To study the seismoelectric transfer function between the electric field and the acceleration, we have to normalize the seismoelectric data with respect to the seismic data. Garambois & Dietrich (2001) normalize the seismoelectric data with the particle acceleration while Dupuis & Butler (2006) use the particle velocity. Mikhailov *et al.* (2000), Singer *et al.* (2005), Zhu *et al.* (2008) and Dorovsky *et al.* (2010) normalize with the pressure, recorded with hydrophones in borehole studies. In addition, Mikhailov *et al.* (2000) and Dupuis & Butler (2006) also use the electrical conductivity to normalize the seismoelectric amplitudes. We achieve the normalization by plotting the amplitude of the seismoelectric signal divided by the amplitude given by the geophone records (actually the amplitude maximum within the time window as described in the beginning of this section).

We also normalize the seismoelectric field with the vertical or horizontal seismic acceleration by taking the time derivative of the geophone records. These two versions of the normalized seismoelectric field are plotted as a function of the resistance of the dipole. The transfer function to calculate the grain velocity from the geophone voltage output was available for the vertical component geophones, but not for the horizontal component geophones. It turned out that these latter ones contained a different damping resistor than indicated in the product specifications and that no transfer function was available for this exact type of geophone. For that reason we calculated the mean of all recorded vertical geophone maxima and the mean of all recorded horizontal geophone maxima. The ratio was used to transfer the voltage output of the horizontal component geophones to horizontal grain velocity using the transfer function for the vertical component geophones. Although the theory shows that the horizontal electrical field is proportional to the horizontal acceleration (see eq. 5), our results show that the highest data quality and the highest similarity with the seismoelectric data can be found on the vertical velocity records. This is not caused by the approximated transfer function of the horizontal component geophones, since this function simply acts as a constant factor in the considered frequency interval.

We automatically determine the time position of the maximum of the envelope for each seismic and each seismoelectric trace. If there is a difference of more than 15 ms in these determined time positions between a seismic trace and its corresponding seismoelectric trace, that trace is not taken into account because in that case seismoelectric and seismic signals could be caused by different phenomena than the theoretical coseismic electric signal caused by the first arrivals of the compressional waves. In Fig. 7 we show the results for the horizontal seismic acceleration, corresponding to 212 analysed traces from both fields (La Soutte and Champ du Feu). Most of the measurements are included in the range 2–12 kΩ and 50–1000 μ Vs^2 m^{-2}. To quantify the seismoelectric amplitudes normalized with respect to the seismic amplitudes as a function of the electrical resistance of the dipoles, we split the statistical study in seven resistance intervals (Fig. 8). We fit the corresponding histogram distribution to a normal law, and deduce an error on each mean value. The errors in normalized amplitude and resistance are used as weights in the weighted linear regression. Resistance regions with less amplitude scattering thus have a greater weight. The regression line is found by minimizing deviations in normalized amplitudes in an iterative manner such as described in, for example, Doerffel & Hebisch (1988).

The resulting regression line and the corresponding equation are shown in Fig. 9. Since the theory predicts that the horizontal electric field is proportional to the horizontal acceleration (see eq. 5), we will focus on this result. The normalizations with the seismic vertical component and the seismic acceleration are summed up in Appendix A. They all show quite similar characteristics and exponents in the regression equations, so the following discussion is largely valid also for those data. Different numbers of resistance intervals yield slightly different regression lines (again, see appendix A). These regression lines from 4, 5 and 7 resistance intervals are shown in Fig. 9(a). We choose a resulting regression line with large enough errors in dip and intercept to include the three different regression lines from Fig. 9(a) (see Fig. 9b). The resulting relation between resistance and the normalized seismoelectric amplitudes is

$$R_{H,\text{der}} = 0.12(\pm 0.19) \left(\frac{E_H}{\ddot{u}_H} \right)^{-2.4(\pm 1.4)}. \tag{11}$$

5 DISCUSSION

Our analysis shows the following relation between the horizontal seismoelectric field measured between two electrodes, the horizontal acceleration measured in the middle of the dipole, and the electrical resistance R measured between the electrodes:

$$\frac{E_H}{\ddot{u}_H} \propto R^{-1/(2.4 \pm 1.4)} \simeq R^{-0.42 \pm 0.25}. \tag{12}$$

During the measurements, the soil was usually quite humid at the surface so that the contact resistance between electrode and soil was quite low. Therefore, the measured resistance R is approximately proportional to the resistivity ρ_r. The resistivity depends on the water saturation S_w as follows (Archie 1942):

$$\rho_r = \frac{\rho_f}{\phi^m S_w^n}, \tag{13}$$

where ρ_f is the fluid resistivity, ϕ the porosity and m and n the Archie exponents (also called cementation exponent and saturation exponent, respectively). Assuming that the porosity and the fluid resistivity are constant, the resistivity is inversely proportional to the water saturation. The electrokinetic coefficient is zero below a residual water saturation S_r, so that it is often described as a function of the effective water saturation

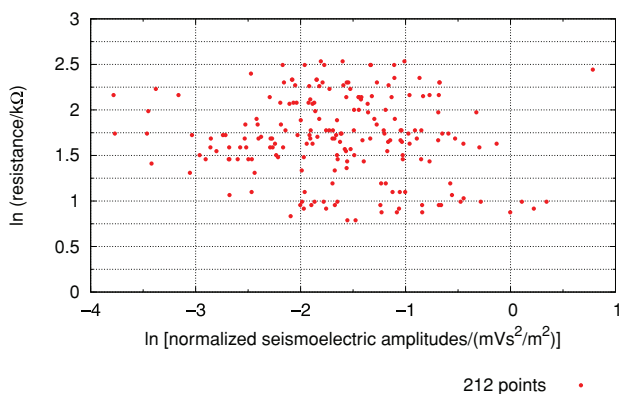$$S_e = \frac{S_w - S_r}{1 - S_r}. \tag{14}$$

Figure 7. Electrical resistance of the dipoles against normalized seismoelectric amplitudes (horizontal seismic acceleration). Both axes are in (natural) logarithmic scale.
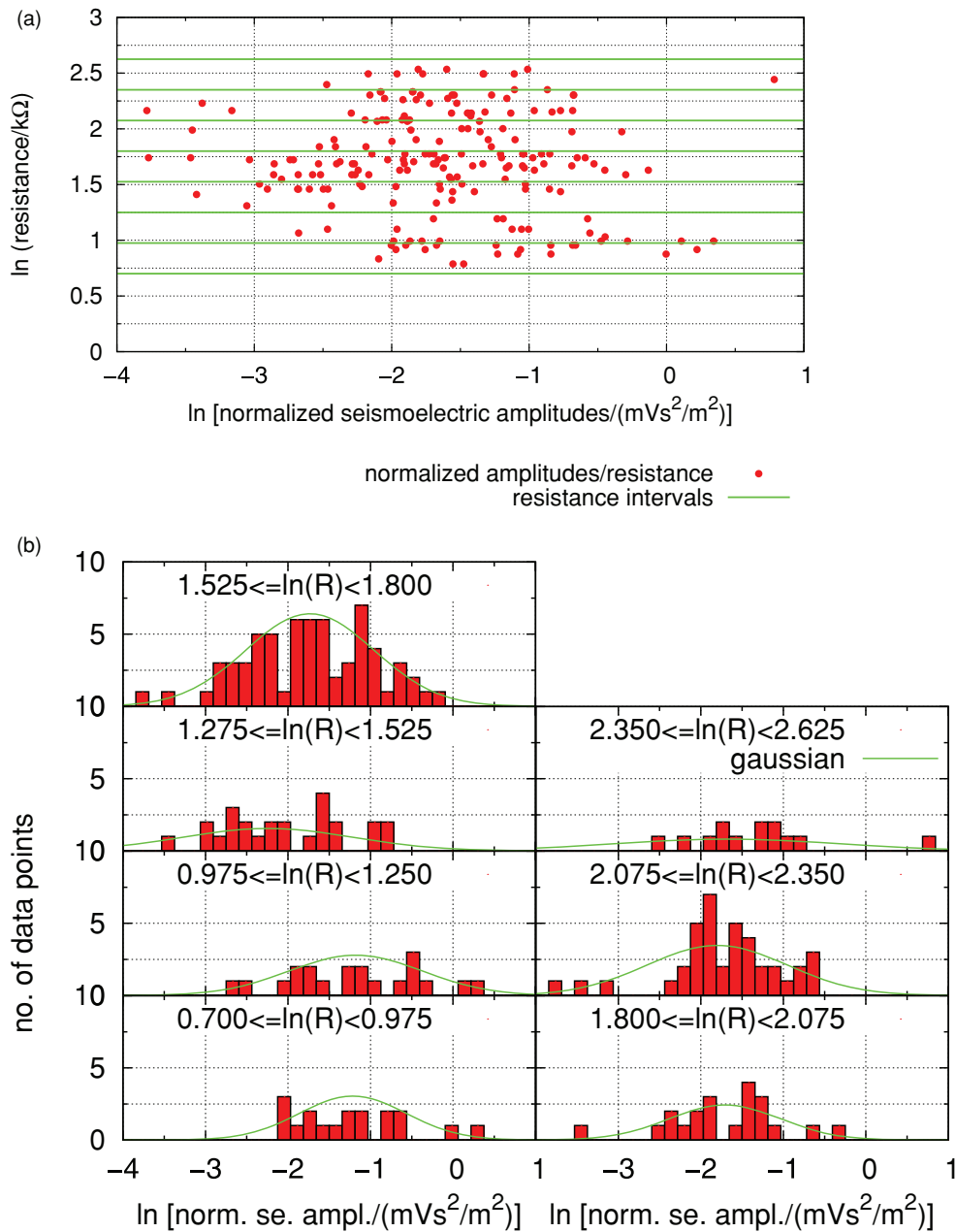
Figure 8. Chosen resistance intervals for the statistical study of the normalized seismoelectric amplitudes (top, green lines), and corresponding histograms fitted with a normal power-law (bottom). The natural logarithm of amplitudes and resistance is used in the diagrams.

This would involve, using eqs (5), (6), (12) and (13)

$$C_s \propto \frac{E_H}{\ddot{u}_H} \propto \rho_r^{-0.42 \pm 0.25} \propto S_e^{(0.42 \pm 0.25)n}. \tag{15}$$

Assuming an electrokinetic coefficient at full water saturation as in eq. (6), we propose that the electrokinetic coefficient depends on water saturation as

$$C_s = \frac{\epsilon \zeta}{\eta \sigma_f} S_e^{(0.42 \pm 0.25)n}. \tag{16}$$

The results of our field study on the seismoelectric amplitude show that the electrokinetic coefficient should increase with water saturation. A laboratory study by Guichet *et al.* (2003) showed also an increase of the electrokinetic coefficient with water saturation,

and some models (Perrier & Morat 2000; Revil *et al.* 2007) proposed an increase of this coefficient, too, but a precise power-law versus water saturation is still in debate. We could hope to expect a common behaviour in porous media without clays or carbonates.

The saturation index n was observed to be about 2 for consolidated rocks and to range from 1.3 to 2 for unconsolidated sands (Schön 1996; Guichet *et al.* 2003; Lesmes & Friedman, 2005). In Fig. 10, we apply eq. (16) with $n = 1.3$ and $n = 2.0$ and compare these curves with the normalized electrokinetic coefficients measured by Guichet *et al.* (2003). The residual saturation S_r (eq. 14) was set to 0.3 as determined in a laboratory drainage experiment in a sand column (Allègre *et al.* 2010). Our study leads to an electrokinetic coefficient dependence on saturation as $S_e^{0.55}$ to $S_e^{0.84}$ (for $n = 1.3$ and $n = 2.0$, respectively). The experimental measurements of Guichet *et al.* (2003) have to be compared to the
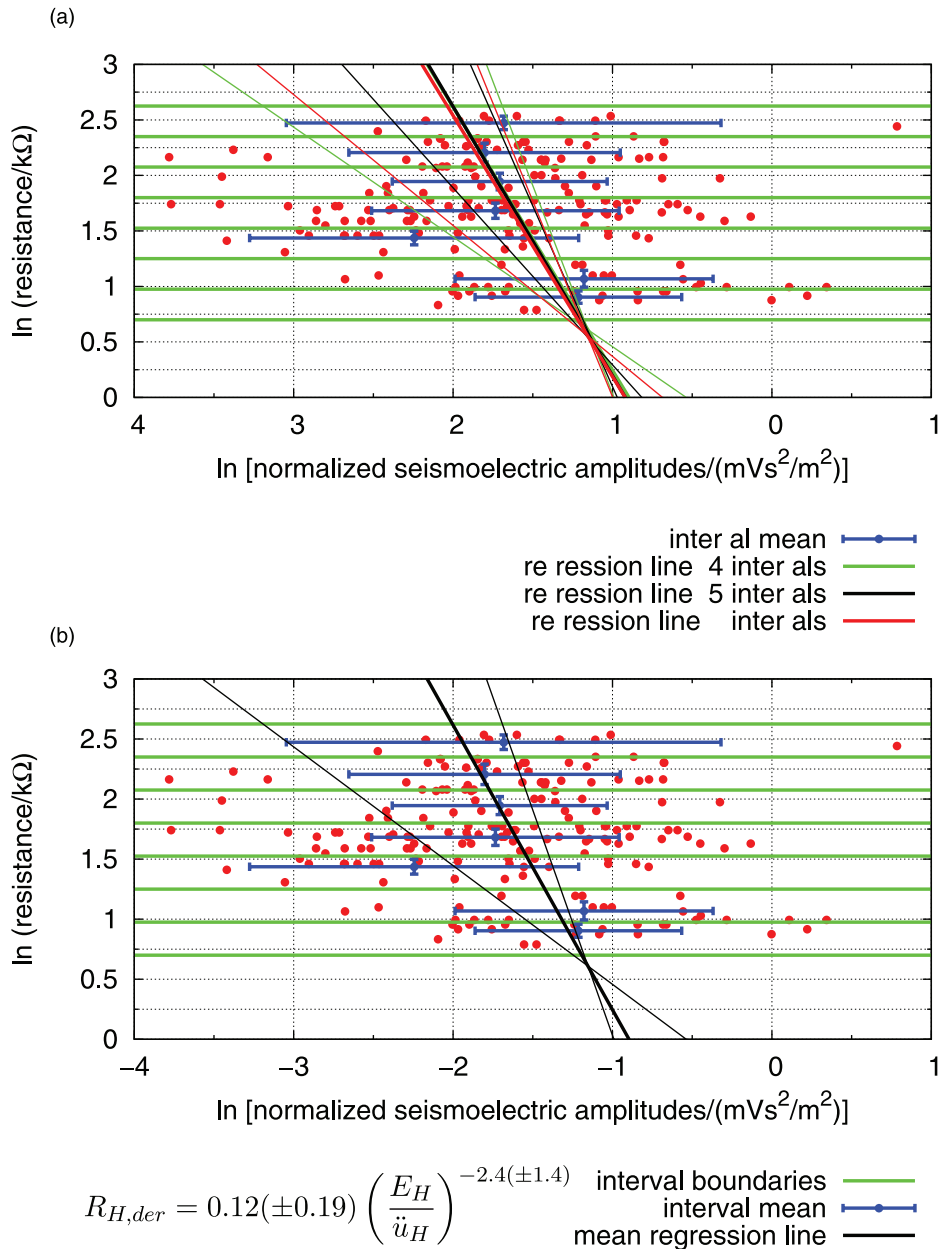
Figure 9. Linear weighted regression of the normalized seismoelectric amplitudes as a function of the electrical resistance (both axes are in natural logarithmic scale). Normalized with respect to the seismic horizontal acceleration: (a) regression lines from analysis with 4, 5 and 7 intervals (see Appendix A), (b) resulting regression line with errors large enough to include all three models from (a).

empirical law using $n = 1.3$ since this experimental study has been performed on sand. A reasonable match between this experimental study and our results can be seen. Also shown are the models of Perrier & Morat (2000) and Revil *et al.* (2007) (see Appendix B for more descriptions). Since they use different values for the residual saturation ($S_r = 0.1$ and $S_r = 0.2$, respectively) and n ($n = 1.0$ in Revil *et al.* 2007), we add their models with $S_r = 0.3$ and $n = 1.3$ as used in this study, as well. The original version of Perrier & Morat (2000) is closest to the measured values of Guichet *et al.* (2003) but they used a very low S_r value of 0.1. The tendency of the remaining curves is the same, with our curve for $n = 1.3$ and the curve of Perrier & Morat (2000) for $S_r = 0.3$ being slightly closer to the values of Guichet *et al.* (2003) than the others. These models were determined with different methods: Perrier & Morat (2000)

postulate their model, Guichet *et al.* (2003) performed laboratory experiments of the streaming potential, the study of Revil *et al.* (2007) is a theoretical one with laboratory experiments for comparison, and we derive the normalized electrokinetic coefficient with seismoelectric field measurements. Keeping this in mind, the match between the different curves is quite good. However we note that in the presence of clays or carbonates this behaviour may be more complex. Finally we show that in the low-frequency domain, taking into account the water saturation, the seismoelectric field and the seismic field are related as

$$\mathbf{E} \simeq \frac{\epsilon \zeta}{\eta \sigma_f} S_e^{(0.42 \pm 0.25)n} \, d_f \, \ddot{\mathbf{u}}. \qquad (17)$$
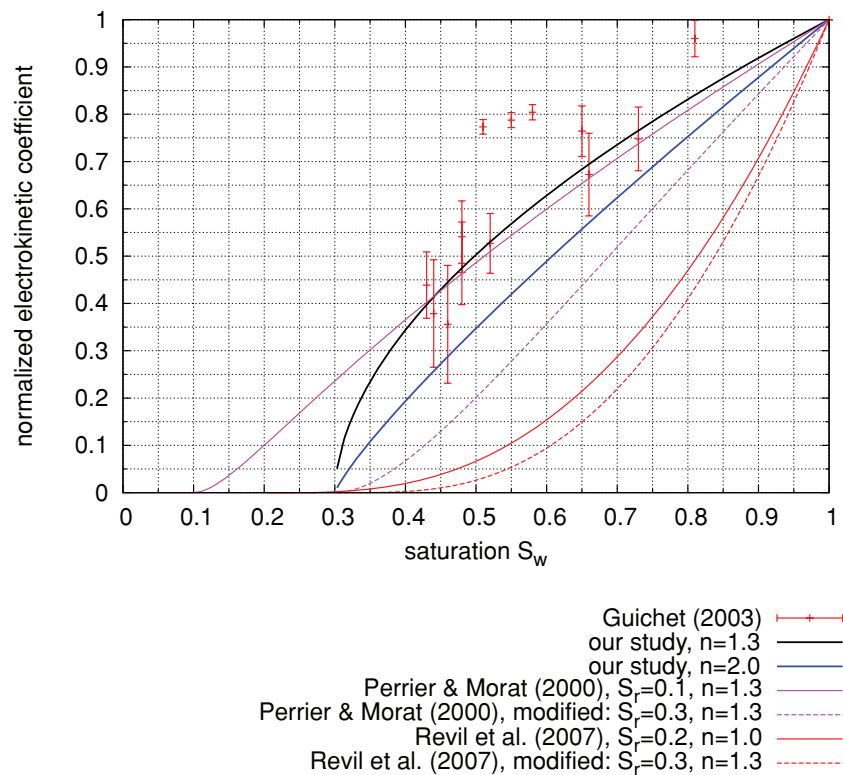
Figure 10. Normalized electrokinetic coefficient versus saturation. Eq. (16) is used with the Archie exponent $n = 1.3$ (black line) and $n = 2.0$ (blue line). The residual saturation S_r (eq. 14) was set to 0.3. These curves are compared with the values measured by Guichet *et al.* (2003) (red dots with error bars). Also shown are the models of Perrier & Morat (2000) (purple) and Revil *et al.* (2007) (red), in their original form (thick solid lines) and with S_r and n adjusted to the values used in this study (thinner dashed lines). In their original version, Perrier & Morat (2000) use $S_r = 0.1$ and $n = 1.3$.

6 CONCLUSION

We show through field measurements that seismoelectric signals were affected by water content. Taking into account the water saturation and assuming the Archie law for the resistivity in non-saturated conditions, the normalized seismoelectric field is a power-law of the effective saturation with the exponent $(0.42 \pm 0.25)n$, where n is Archie's saturation exponent (see eq. 17). Further studies are needed to improve our understanding of these phenomena. The electrical resistance investigated in this study was restricted to relatively low values such as 5–20 kΩ, corresponding to a relatively high water saturation. A complementary study with higher values of resistance would improve our results and a comparison with detailed laboratory experiments should improve our understanding of these phenomena.

REFERENCES

Adam, E. & Langlois, P., 1995. Elimination of monofrequency noise from seismic records, *Lithoprobe Seismic Processing Facility Newsletter*, **8**, 59–65.

Adamson, A.W., 1976. *Physical Chemistry of Surfaces*, John Wiley and sons, New York, NY.

Adler, P.M., Thovert, J.F., Jacquin, C., Morat, P. & Le Mouël, J.L., 1997. Electrical signals induced by the atmospheric pressure variations in unsaturated media, *C.R. Acad. Sci. Paris*, **324**, 711–718.

Ageeva, O.A., Svetov, B.S., Sherman, G.K. & Shipulin, V., 1999. E-effect in rocks, *Russian Geol. Geophys.*, **64**, 1349–1356.

Allègre, V., Jouniaux, L., Lehmann, F. & Sailhac, P., 2010. Streaming Potential dependence on water-content in Fontainebleau Sand, *Geophys. J. Int.*, **182**, 1248–1266.

Archie, G.E., 1942. The electrical resistivity log as an aid in determining some reservoir characteristics, *Trans. Am. Inst. Min. Metall. Pet. Eng.*, **146**, 54–62.

Aubert, M. & Atangana, Q.Y., 1996. Self-potential method in hydrogeological exploration of volcanic areas, *Ground Water*, **34**, 1010–1016.

Beamish, D., 1999. Characteristics of near surface electrokinetic coupling, *Geophys. J. Int.*, **137**, 231–242.

Biot, M.A., 1956. Theory of propagation of elastic waves in a fluid-saturated porous solid: I. Low frequency range, *J. acoust. Soc. Am.*, **28**(2), 168–178.

Block, G.I. & Harris, J.G., 2006. Conductivity dependence of seismoelectric wave phenomena in fluid-saturated sediments, *J. geophys. Res.*, **111**, B01304, doi:10.1029/2005JB003798.

Bordes, C., Jouniaux, L., Dietrich, M., Pozzi, J.-P. & Garambois, S., 2006. First laboratory measurements of seismo-magnetic conversions

in fluid-filled Fontainebleau sand, *Geophys. Res. Lett.*, **33**, L01302, doi:10.1029/2005GL024582.

Bordes, C., Jouniaux, L., Garambois, S., Dietrich, M., Pozzi, J.-P. & Gaffet, S., 2008. Evidence of the theoretically predicted seismo-magnetic conversion, *Geophys. J. Int.*, **174**, 489–504.

Butler, K., 1996. Seismoelectrics effects of electrokinetic origin, *PhD thesis*, Univ. British Columbia, Vancouver.

Butler, K.E. & Russell, R.D., 1993. Substraction of powerline harmonics from geophysical records, *Geophysics*, **58**, 898–903.

Butler, K.E. & Russell, R.D., 2003. Cancellation of multiple harmonic noise series in geophysical records, *Geophysics*, **68**, 1083–1090.

Chandler, R., 1981. Transient streaming potential measurements on fluid-saturated porous structures: an experimental verification of Biot's slow wave in the quasi-static limit, *J. acoust. Soc. Am.*, **70**, 116–121.

Chen, B. & Mu, Y., 2005. Experimental studies of seismoelectric effects in fluid-saturated porous media, *J. geophys. Eng.*, **2**, 222–230.

Cooke, C.E., 1955. Study of electrokinetic effects using sinusoidal pressure and voltage, *J. Chem. Phys.*, **23**, 2299–2303.

Darnet, M. & Marquis, G., 2004. Modelling streaming potential (sp) signals induced by water movement in the vadose zone, *J. Hydrol.*, **285**, 114–124.

Davis, J.A., James, R.O. & Leckie, J., 1978. Surface ionization and complexation at the oxide/water interface, *J. Colloid Interface Sci.*, **63**, 480–499.

Doerffel, K. & Hebisch, R., 1988. Nachweis systematischer Fehler durch gewichtete Regression, *Fresenius Z Anal Chem*, **331**(5), 510–512.

Dorovsky, V., Nefedkin, Y., Fedorov, A. & Podberezhnyy, M., 2010. A logging method for estimating permeability, velocity of second compressional wave, and electroacoustic constant in electrolyte-saturated porous formations, *Russian Geol. Geophys.*, **51**(12), 1285–1294.

Dullien, F., 1992. *Porous Media: Fluid Transport and Pore Structure*, Academic Press, San Diego, CA.

Dupuis, J.C. & Butler, K.E., 2006. Vertical seismoelectric profiling in a borehole penetrating glaciofluvial sediments, *Geophys. Res. Lett.*, **33**, L16301, doi:10.1029/2006GL026385.

Dupuis, J.C., Butler, K.E. & Kepic, A.W., 2007. Seismoelectric imaging of the vadose zone of a sand aquifer, *Geophysics*, **72**, A81–A85.

Dupuis, J.C., Butler, K.E., Kepic, A.W. & Harris, B.D., 2009. Anatomy of a seismoelectric conversion: measurements and conceptual modeling in boreholes penetrating a sandy aquifer, *J. geophys. Res.*, **114**, B10306, doi:10.1029/2008JB005939.

Garambois, S. & Dietrich, M., 2001. Seismoelectric wave conversions in porous media: field measurements and transfer function analysis, *Geophysics*, **66**, 1417–1430.

Garambois, S. & Dietrich, M., 2002. Full waveform numerical simulations of seismoelectromagnetic wave conversions in fluid-saturated stratified porous media, *J. geophys. Res.*, **107**(B7), ESE 5–1.

Gibert, D. & Pessel, M., 2001. Identification of sources of potential fields with the continuous wavelet transform: application to self-potential profiles, *Geophys. Res. Lett.*, **28**, 1863–1866.

Gorsy, P., Hulin, G., Knobel, P., Sanchez, O., Thiebaut, C., Valois, R. & Wawrzyniak, P., 2006. Rapport de synthèse, Champ du Feu, *Rapport de Stage,* Université Louis Pasteur de Strasbourg, pp. 1–39.

Guichet, X. & Zuddas, P., 2003. Effect of secondary minerals on electrokinetic phenomena during water-rock intercation, *Geophys. Res. Lett.*, **30**, 1714, doi:10.1029/2003GL017480.

Guichet, X., Jouniaux, L. & Pozzi, J.-P., 2003. Streaming potential of a sand column in partial saturation conditions, *J. geophys. Res.*, **108**(B3), 2141, doi:10.1029/2001JB001517.

Guichet, X., Jouniaux, L. & Catel, N., 2006. Modification of streaming potential by precipitation of calcite in a sand-water system: laboratory measurements in the pH range from 4 to 12, *Geophys. J. Int.*, **166**, 445–460.

Haartsen, M.W. & Pride, S., 1997. Electroseismic waves from point sources in layered media, *J. geophys. Res.*, **102**, 24 745–24 769.

Haartsen, M.W., Dong, W. & Toksöz, M.N., 1998. Dynamic streaming currents from seismic point sources in homogeneous poroelastic media, *Geophys. J. Int.*, **132**, 256–274.

Haines, S.S., Guitton, A. & Biondi, B., 2007a. Seismoelectric data processing for surface surveys of shallow targets, *Geophysics*, **72**, G1–G8.

Haines, S.S., Pride, S.R., Klemperer, S.L. & Biondi, B., 2007b. Seismoelectric imaging of shallow targets, *Geophysics*, **72**, G9–G20.

Henry, P., Jouniaux, L., Screaton, E.J., Hunze, S. & Saffer, D.M., 2003. Anisotropy of electrical conductivity record of initial strain at the toe of the Nankai accretionary wedge, *J. geophys. Res.*, **108**, 2407, doi:10.1029/2002JB002287.

Hunt, C.W. & Worthington, M.H., 2000. Borehole elektrokinetic responses in fracture dominated hydraulically conductive zones, *Geophys. Res. Lett.*, **27**(9), 1315–1318.

Hunter, R., 1981. *Zeta Potential in Colloid Science: Principles and Applications*, Academic, New York, NY.

Ishido, T. & Mizutani, H., 1981. Experimental and theoretical basis of electrokinetic phenomena in rock water systems and its applications to geophysics, *J. geophys. Res.*, **86**, 1763–1775.

Jaafar, M.Z., Vinogradov, J. & Jackson, M.D., 2009. Measurement of streaming potential coupling coefficient in sandstones saturated with high salinity nacl brine, *Geophys. Res. Lett.*, **36**, L21306, doi:10.1029/2009GL040549.

Jouniaux, L., Lallemant, S. & Pozzi, J., 1994. Changes in the permeability, streaming potential and resistivity of a claystone from the Nankai prism under stress, *Geophys. Res. Lett.*, **21**, 149–152.

Jouniaux, L., Pozzi, J.-P., Berthier, J. & Massé, P., 1999. Detection of fluid flow variations at the Nankai trough by electric and magnetic measurements in boreholes or at the seafloor, *J. geophys. Res.*, **104**, 29 293–29 309.

Jouniaux, L., Bernard, M.-L., Zamora, M. & Pozzi, J.-P., 2000. Streaming potential in volcanic rocks from Mount Peleé, *J. geophys. Res.*, **105**, 8391–8401.

Jouniaux, L., Zamora, M. & Reuschlé, T., 2006. Electrical conductivity evolution of non-saturated carbonate rocks during deformation up to failure, *Geophys. J. Int.*, **167**, 1017–1026.

Lesmes, D.P. & Friedman, S.P., 2005. Relationships between the electrical and hydrogeological properties of rocks and soils, in *Hydrogeophysics*, ch. 4, pp. 87–128, eds Rubin, Y. & Hubbard, S.S., Springer, Dordrecht.

Long, L.T. & Rivers, W.K., 1975. Field measurement of the electroseismic response, *Geophysics*, **40**, 233–245.

Lorne, B., Perrier, F. & Avouac, J.-P., 1999. Streaming potential measurements. 1. Properties of the electrical double layer from crushed rock samples, *J. geophys. Res.*, **104**(B8), 17 857–17 877.

Maineult, A., Strobach, E. & Renner, J., 2008. Self-potential signals induced by periodic pumping, *J. geophys. Res.*, **113**, B01203, doi:10.1029/2007JB005193.

Martner, S.T. & Sparks, N.R., 1959. The electroseismic effect, *Geophysics*, **24**(2), 297–308.

Mikhailov, O.V., Queen, J. & Toksöz, M.N., 2000. Using borehole electroseismic measurements to detect and characterize fractured (permeable) zones, *Geophysics*, **65**, 1098–1112.

Minsley, B.J., Sogade, J. & Morgan, F.D., 2007. Three-dimensional self-potential inversion for subsurface DNAPL contaminant detection at the Savannah river site, South Carolina, *Water Resour. Res.*, W04429, doi:10.1029/2005WR003996.

Mironov, S.A., Parkhomenko, E.I. & Chernyak, G.Y., 1994. Seismoelectric effect in rocks containing gas or fluid hydrocarbon (English translation), *Izv. Phys. Solid Earth*, **29**(11), 1000–1006.

Packard, R.G., 1953. Streaming potentials across capillaries for sinusoidal pressure, *J. Chem. Phys*, **1**(21), 303–307.

Parkhomenko, E. & Gaskarov, I., 1971. Borehole and laboratory studies of the seismoelectric effect of the second kind in rocks, *Izv. Akad. Sci. USSR, Physics Solid Earth*, **9**, 663–666.

Parkhomenko, I. & Tsze-San, C., 1964. A study of the influence of moisture on the magnitude of the seismoelectric effect in sedimentary rocks by a laboratory method, *Bull. (Izv.) Acad. Sci., USSR, Geophys. Ser.*, **2**, 115–118.

Perrier, F. & Morat, P., 2000. Characterization of electrical daily variations induced by capillary flow in the non-saturated zone, *Pure appl. Geophys.*, **157**, 785–810.

Perrier, F., Trique, M., Lorne, B., Avouac, J.-P., Hautot, S. & Tarits, P., 1998. Electric potential variations associated with lake variations, *Geophys. Res. Lett.*, **25**, 1955–1958.

Pinettes, P., Bernard, P., Cornet, F., Hovhannissian, G., Jouniaux, L., Pozzi, J.-P. & Barthés, V., 2002. On the difficulty of detecting streaming potentials generated at depth, *Pure appl. Geophys.*, **159**, 2629–2657.

Pozzi, J.-P. & Jouniaux, L., 1994. Electrical effects of fluid circulation in sediments and seismic prediction, *C.R. Acad. Sci. Paris, serie II*, **318**(1), 73–77.

Pride, S., 1994. Governing equations for the coupled electromagnetics and acoustics of porous media, *Phys. Rev. B: Condens. Matter*, **50**, 15 678–15 695.

Reppert, P. & Morgan, F., 2003a. Temperature-dependent streaming potentials: 1. Theory, *J. geophys. Res.*, **108**, 2546, doi:10.1029/2002JB001754.

Reppert, P. & Morgan, F., 2003b. Temperature-dependent streaming potentials: 2. Laboratory, *J. geophys. Res.*, **108**, 2547, doi:10.1029/2002JB001755.

Reppert, P.M., Morgan, F.D., Lesmes, D.P. & Jouniaux, L., 2001. Frequency-dependent streaming potentials, *J. Colloid Interface Sci.*, **234**, 194–203.

Revil, A., Linde, N., Cerepi, A., Jougnot, D., Matthäi, S. & Finsterle, S., 2007. Electrokinetic coupling in unsaturated porous media, *J. Colloid Interface Sci.*, **313**, 315–327.

Sailhac, P., Darnet, M. & Marquis, G., 2004. Electrical streaming potential measured at the ground surface: forward modeling and inversion issues for monitoring infiltration and characterizing the vadose zone, *Vadose Zone J.*, **3**, 1200–1206.

Sailhac, P. *et al.*, 2009. Characterizing vadose zone and perched aquifer near Vosgian ridges in La Soutte experimental site, Obernai, France, *C.R. Geosci.*, **341**, 818–830.

Saracco, G., Labazuy, P. & Moreau, F., 2004. Localization of self-potential sources in volcano-electric effect with complex continuous wavelet transform and electrical tomography methods for an active volcano, *Geophys. Res. Lett.*, **31**, L12610, doi:10.1029/2004GL019554.

Saunders, J.H., Jackson, M.D. & Pain, C.C., 2006. A new numerical model of electrokinetic potential response during hydrocarbon recovery, *Geophys. Res. Lett.*, **33**, L15316, doi:10.1029/2006GL026835.

Schoemaker, F., Smeulders, D. & Slob, E., 2008. Electrokinetic effect: theory and measurement, *SEG Expanded Abstracts*, **27**, 1645–1649.

Schön, J., 1996. Physical properties of rocks: fundamentals and principles of petrophysics, in *Handbook of Geophysical Exploration, Seismic Exploration*, Vol. 18, Elsevier Science Ltd, New York, NY.

Sill, W., 1983. Self-potential modeling from primary flows, *Geophysics*, **48**, 76–86.

Singer, J., Saunders, J., Holloway, L., Stoll, J., Pain, C., Stuart-Bruges, W. & Mason, G., 2005. Electrokinetic logging has the potential to measure the permeability, in *Proceedings of 46th Annual Logging Symposium*, Society of Petrophysicists and Well Log Analysts.

Strahser, M.H.P., 2007. Near surface seismoelectrics in comparative field studies, *PhD thesis*, Christian-Albrechts-Universität zu Kiel, Kiel.

Strahser, M.H.P., Rabbel, W. & Schildknecht, F., 2007. Polarisation and slowness of seismoelectric signals: a case study, *Near Surf. Geophys.*, **5**, 97–114.

Thompson, A. *et al.*, 2005. Field tests of electroseismic hydrocarbon detection, *SEG Expanded Abstracts*, **24**, 565–568.

Thompson, A., Sumner, J. & Hornbostel, S., 2007. Electromagnetic-to-seismic conversion: a new direct hydrocarbon indicator, *Leading Edge*, **43**, 428–435.

Thompson, R.R., 1936. The seismic-electric effect, *Geophysics*, **1**(3), 327–335.

Zhu, Z. & Toksöz, M.N., 2003. Crosshole seismoelectric measurements in borehole models with fractures, *Geophysics*, **68**(5), 1519–1524.

Zhu, Z., Haartsen, M.W. & Toksöz, M.N., 1999. Experimental studies of electrokinetic conversions in fluid-saturated borehole models, *Geophysics*, **64**, 1349–1356.

Zhu, Z., Toksöz, M.N. & Burns, D.R., 2008. Electroseismic and seismoelectric measurements of rock samples in a water tank, *Geophysics*, **73**, E153–E164, doi:10.1190/1.2952570.

APPENDIX A: REGRESSION RESULTS FOR DIFFERENT INTERVAL NUMBERS

In Fig. 9, we presented a linear weighted regression of the normalized seismoelectric amplitudes as a function of the electrical resistance. Since it is necessary to have a uniform sampling for a regression in log–log scale, we subdivided the range of the measured resistivities into several intervals. Different numbers of intervals yield slightly different regression lines. We show here the results of a weighted least-squares regression for 4, 5 and 7 intervals (Figs A1–A3, respectively). This gives us an indication of the uncertainties of the final result. The seismoelectric data (horizontal component) are normalized with respect to seismic data in four versions: the seismic vertical and horizontal components and in each case the original form of the data (velocity) and the first derivative in time (acceleration). As explained in Section 2.3, Garambois & Dietrich (2001) showed that the seismoelectric (coseismic) signal is proportional to the ground acceleration, that is, the time derivative of the horizontal geophone output. However, we analyse all four possible combinations here since field observations sometimes showed a greater similarity between the seismoelectric horizontal component and the seismic vertical component, often in the non-derived form.

In general, the regression lines of the different interval models do not differ much. As explained in Section 4.2, it is mainly the exponent of the regression equation that we are interested in. We follow a careful approach and choose to incorporate the results of all three models with different intervals into the exponent, which gives us $E_H/\dot{u}_V \propto R^{-1/(2.0\pm0.9)} \simeq R^{-0.49\pm0.21}$ for normalization with the vertical seismic component, $E_H/\dot{u}_H \propto R^{-1/(2.7\pm2.5)} \simeq R^{-0.37\pm0.34}$ with the horizontal seismic component, $E_H/\ddot{u}_V \propto R^{-1/(1.7\pm0.6)} \simeq R^{-0.58\pm0.21}$ with the time-derived vertical seismic component and $E_H/\ddot{u}_H \propto R^{-1/(2.4\pm1.4)} \simeq R^{-0.42\pm0.25}$ with the time-derived horizontal seismic component. In Section 5, we refer to the seismoelectric amplitudes normalized with the time-derived horizontal seismic amplitudes but as can be seen, the other exponents are quite similar. In fact, the exponent of each of the four normalization variants lies in the error range of the others, so the discussion in Section 4.2 is largely valid for all four normalization variants.

APPENDIX B: MODELS OF PERRIER & MORAT (2000) AND REVIL ET AL. (2007)

In Fig. 10 we compare the behaviour of the normalized electrokinetic coefficient against saturation as predicted by our experimentally derived law (eq. 15) with two other models proposed in literature. Perrier & Morat (2000) suggest (in the notation used in this paper)

$$\frac{C_s}{C_s^0} = \frac{S_e^2}{S_w^n}, \tag{B1}$$

with C_s^0: electrokinetic coefficient at full saturation, and n: Archie's saturation exponent. These authors use $n = 2$. Following Adler *et al.* (1997) who cite Dullien (1992), they set the residual saturation to $S_r = 0.1$.

Revil *et al.* (2007) use

$$\frac{C_s}{C_s^0} = \frac{S_e^{(2+3\lambda)/\lambda}}{S_w^{n+1}}, \tag{B2}$$

where λ is a curve-shape parameter corresponding to an index for the pore space distribution. A typical value for sand is $\lambda = 1.7$. Also for sand, Revil *et al.* (2007) use $S_r = 0.2$ and $n = 1.0$.
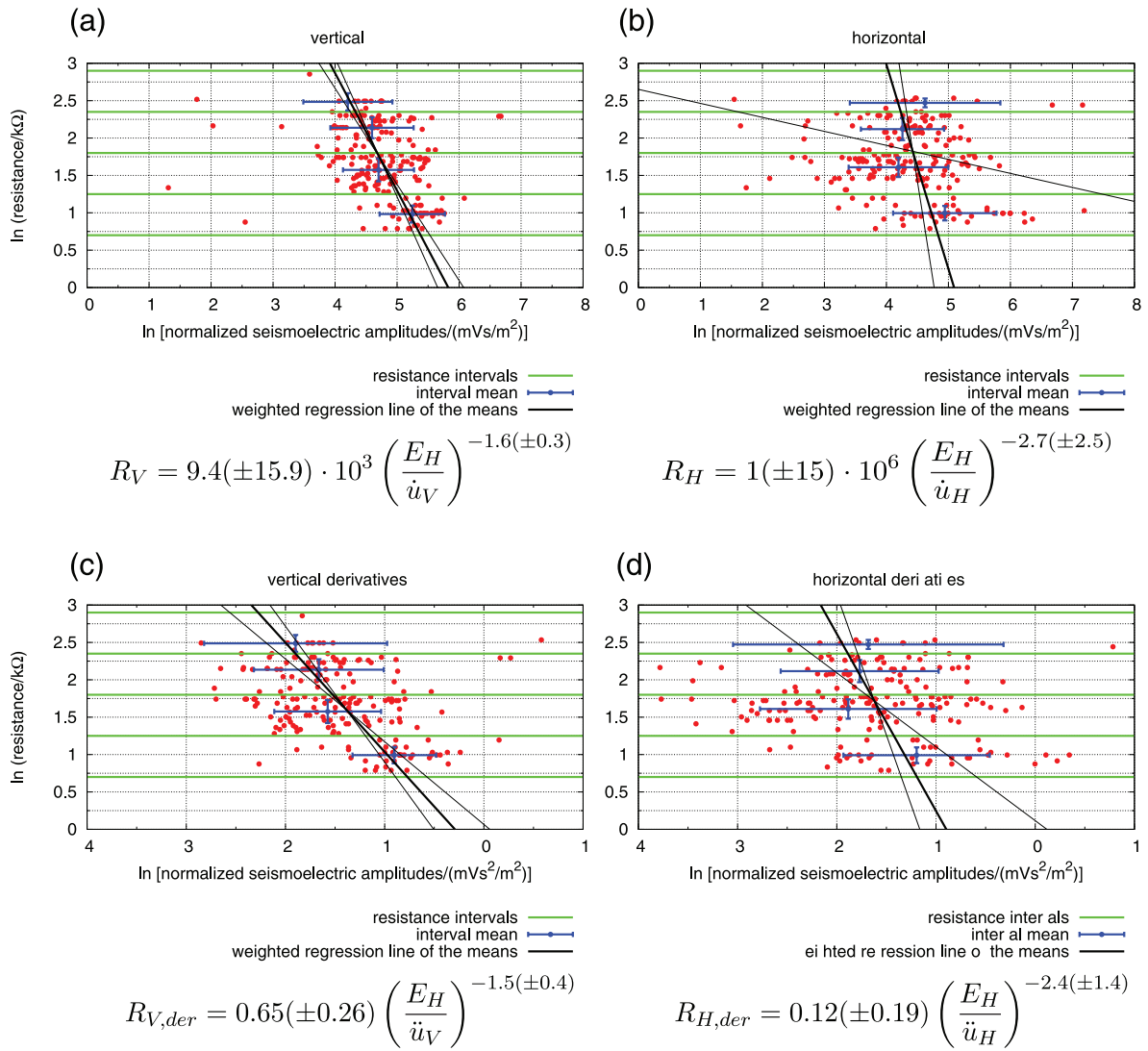
Figure A1. Linear weighted regression of the normalized seismoelectric amplitudes as a function of the electrical resistance (both axes in natural logarithmic scale). Normalized with respect to the seismic vertical velocity (a), the seismic horizontal velocity (b), the seismic vertical acceleration (c) and the seismic horizontal acceleration (d). The resistance values are grouped into four intervals.
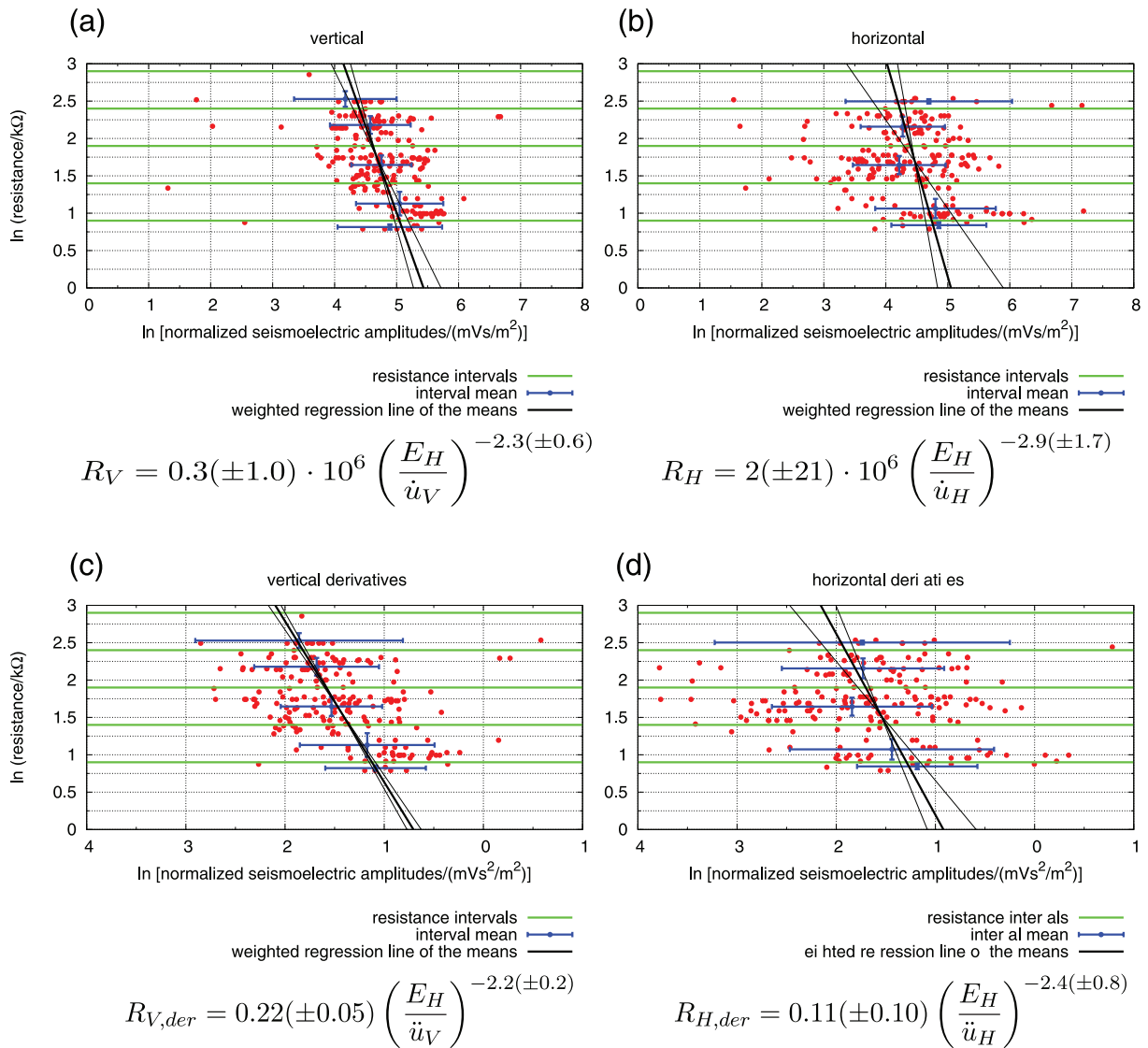
Figure A2. Linear weighted regression of the normalized seismoelectric amplitudes as a function of the electrical resistance (both axes in natural logarithmic scale). Normalized with respect to the seismic vertical velocity (a), the seismic horizontal velocity (b), the seismic vertical acceleration (c), and the seismic horizontal acceleration (d). The resistance values are grouped into 5 intervals.
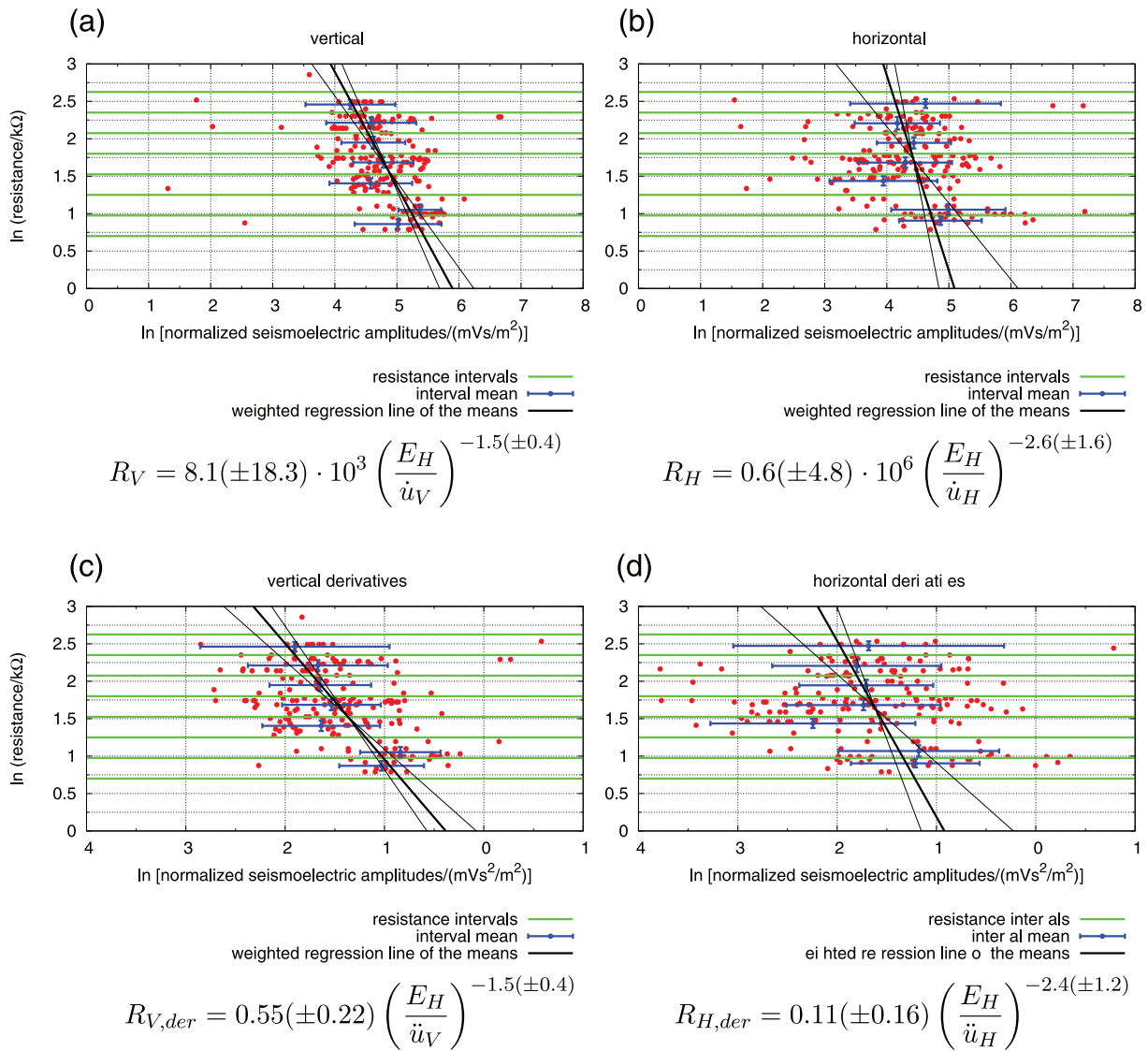
Figure A3. Linear weighted regression of the normalized seismoelectric amplitudes as a function of the electrical resistance (both axes in natural logarithmic scale). Normalized with respect to the seismic vertical velocity (a), the seismic horizontal velocity (b), the seismic vertical acceleration (c) and the seismic horizontal acceleration (d). The resistance values are grouped into seven intervals.